



TECHNICAL ARTICLE

Effect of Cold Rolling on the Microstructure Evolution, Mechanical, and Corrosion Properties of AlCoCrFeNi_{2.4} High-Entropy Alloy

Mehrab Seifpour Bijnavandi, Armin Ghaderi , and Kamran Dehghani

Submitted: 6 September 2022 / Revised: 6 February 2023 / Accepted: 4 March 2023 / Published online: 29 March 2023

This study investigates the microstructure, mechanical, and corrosion properties of as-cast and cold-rolled AlCoCrFeNi_{2.4} high-entropy alloy at room temperature. The microstructure is examined using x-ray diffraction (XRD) and scanning electron microscopy (SEM) equipped with energy-dispersive x-ray spectroscopy (EDS). X-ray diffraction (XRD) analysis revealed that the constituent phases in the as-cast sample were FCC and BCC. The as-cast microstructure was observed to contain a primary FCC dendrite and a secondary FCC ($L1_2$) + BCC (B_2) typical hyper-eutectic structure in the interdendritic region. Furthermore, the cold-rolled microstructure was severely deformed along the cold rolling direction. With the increase in thickness reduction from cold rolling, the microhardness, yield strength, shear strength, and ultimate strength of the alloy all increased, despite a decrease in ductility. Moreover, after the alloy was cold-rolled to 90%, the alloy demonstrated yield strengths of 1791 MPa, ultimate tensile strengths of 1956 MPa, and elongation to fracture values of 10.17%. In addition to these results, the as-cast sample demonstrated excellent corrosion resistance in a NaCl-based solution.

Keywords cold rolling, high-entropy alloy, mechanical behavior, microstructure

1. Introduction

During the last decade, high-entropy alloys (HEAs), also known as multi-principal-element alloys, have received considerable attention (Ref 1, 7). This type of alloy is defined as an alloy containing at least four significant or principal elements whose proportions are equiatomic or virtually equiatomic (Ref 2-6). In the early stages of HEA research, single-phase solid solutions with intriguing properties, such as high strength (Ref 8-10) and high plasticity at room temperature (Ref 11-13), were the primary focus. In recent years, a wide range of HEA systems have been developed and shown to have various exceptional properties, including high strength (Ref 14, 15), high plasticity (Ref 16), corrosion resistance (Ref 17), wear resistance (Ref 18, 19), and exceptional cryogenic and elevated temperature properties (Ref 20, 21).

Dual-phase alloys have undergone extensive research and development to obtain high-entropy alloy, which is advantageous for increased strength and excellent ductility (Ref 22, 23). Eutectic HEAs (EHEA) have improved properties and

superior castability, distinguishing them as a special class of HEA (Ref 24). The literature has evidenced that AlCoCrFeNi_{2.1} EHEA possesses superior mechanical properties due to the existence of ordered $L1_2$ (soft) and B_2 (hard) phases (Ref 24, 25). A study of the as-cast EHEA at room temperature demonstrated high tensile ductility and high fracture strength (Ref 26). The as-cast EHEA is characterized by a fine $L1_2/B_2$ lamellar microstructure and exhibits unprecedented tensile ductility and fracture strength (Ref 26).

Guo et al. (Ref 27) reported that with the increase in Al content, a phase transition from the FCC to BCC occurs in the Al_xCrCuFeNi₂ system. Ma et al. (Ref 28) investigated phase stability, microstructural evolution, microhardness, and compression performance of Al_xCrCuFeNi₂ HEAs in as-cast and annealed forms. Moreover, Lu et al. (Ref 29) developed eutectic and near-eutectic AlCoCrFeNi_x ($X = 2.0, 2.1, 2.2$) HEAs and studied their mechanical properties at room temperature and low temperatures. Zhang et al. (Ref 30) investigated the deformation mechanism of the eutectic AlCoCrFeNi_{2.1} alloy assessed under high-temperature tensile conditions. The results indicated that precipitation hardening and dynamic recrystallization occurred simultaneously at 1000 °C, causing the ultimate tensile strength and yield strength of the material to decrease with increasing temperature, while the opposite is true for elongation. Wang et al. (Ref 31) demonstrated that AlCoCrFeNiTi_{0.5} HEA has a high compressive strength of 2.26 GPa at room temperature and fracture strength of up to 3.14 GPa, demonstrating a high plasticity of up to 23.3% under compression.

Due to its unique properties, AlCoCrFeNi_{2.4} HEA is a highly desirable material that possesses both ductility and strength. To this end, AlCoCrFeNi_{2.4} HEA has been extensively studied due to its exceptional properties and suitability for numerous applications. However, the effects of HEAs after

Armin Ghaderi and Mehrab Seifpour Bijnavandi have contributed equally to this work as first authors.

Mehrab Seifpour Bijnavandi, Armin Ghaderi, and Kamran Dehghani, Department of Materials and Metallurgical Engineering, Amirkabir University of Technology, Tehran, Iran. Contact e-mail: ghaderiarmin5@gmail.com.

cold rolling have not been studied exhaustively. Furthermore, $\text{AlCoCrFeNi}_{2.4}$ has not been studied in depth where HEA is simultaneously obtained under two different conditions (as-cast, cold-rolled).

To investigate microstructural evolution, we examined the microstructural evolution of $\text{AlCoCrFeNi}_{2.4}$ HEA after cold rolling as part of this study. During the investigation, the tensile properties of the cold-rolled alloy were also characterized. In this work, $\text{AlCoCrFeNi}_{2.4}$ HEA was analyzed to determine the microstructural and mechanical changes, corrosion resistance, and fracture properties resulting from being obtained under two distinct states.

2. Materials and Methods

$\text{AlCoCrFeNi}_{2.4}$ HEA ingots were obtained using vacuum arc remelting (VAR) under a 3×10^{-4} mbar vacuum. Elements with over 99 wt.% purity were utilized as raw materials. Four consecutive remelting procedures were performed to improve the chemical homogeneity of the ingots to meet the required chemical homogeneity. The dimensions of produced ingot were $8 \times 25 \times 140$ mm. The alloy's final thickness of 0.75 mm was achieved through seven passes of cold rolling, i.e., 90% reduction. After cold rolling, the specimens were cut into dog-bone specimens using Wire Electrical Discharge Machining (WEDM) and per JISSZ2201, as shown in Fig. 1. According to Table 1, the chemical composition of the investigated alloy closely resembles the nominal composition of $\text{AlCoCrFeNi}_{2.4}$, as determined by a Philips X Unique II XRF machine.

After grinding the samples, they were polished mechanically before being etched in Marble's Reagent (10 gr $\text{CuSO}_4 + 50$ ml $\text{HCl} + 50$ ml H_2O). A Rigaku Ultima IV diffractometer employing $\text{Cu } K_\alpha$ radiation was utilized to characterize the phase structure of the material through x-ray diffraction analysis. Microstructural observations and the internal characteristics of the alloy were determined via scanning electron microscope (SEM-Tescan VEGA II) with energy-dispersive x-ray spectroscopy (EDS) illumination. Tensile testing was performed at a strain rate of 10^{-3} s^{-1} under room temperature.

An extensometer was employed to measure the tensile properties of the material. Before tensile testing, the samples were mechanically polished to eliminate the effects of cold rolling due to any possible impact of concentrated surface stress on their tensile strength. Sample preparation for Shear punch testing (SPT) was performed in compliance with ASTM D732 standard procedures. Shear punch testing (SPT) was conducted using a flat punch with a diameter of 3 mm at a crosshead speed of 0.2 mm/s. The thickness of the samples was 1.5 mm. Afterward, the stress–elongation curves were plotted using the recorded machine force–displacement data through Eq 1:

$$\tau = \frac{P}{2\pi r t} \quad (\text{Eq 1})$$

where τ , p , r , and t denote the shear stress, load, average radius of the punch and lower dies, and specimen thickness, respectively.

The average hardness value was calculated using a Vickers hardness tester with a 50 gr load. Each sample's average hardness was determined by measuring it at least five times. Potentiodynamic polarization curves were obtained to study the

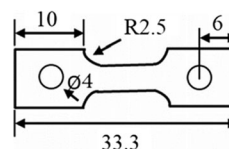


Fig. 1 Illustration of the tensile sample (dimensions in mm)

Table 1 Chemical composition of the investigated alloy

Element	Al	Co	Cr	Fe	Ni
at.%	15.54	15.26	15.63	15.84	37.73

corrosion behavior of the studied alloy. The test was conducted in a 3.5% NaCl solution using three electrodes at room temperature (CHI660 D), with the Ag/AgCl electrode serving as the reference electrode, the silver electrode serving as the auxiliary electrode, and the $\text{AlCoCrFeNi}_{2.4}$ alloy as the working electrode. The corrosion behavior of specimens was evaluated using a 400 mV potential scan range, a submerged specimen, and a scanning rate of 10 mV/s.

3. Results and Discussion

3.1 X-ray Diffraction Analysis

Figure 2 illustrates the XRD patterns of the $\text{AlCoCrFeNi}_{2.4}$ alloy in both as-cast and cold-rolled states. A combination of FCC and BCC dual phases was present in the as-cast $\text{AlCoCrFeNi}_{2.4}$ alloy. It is evident that the intensity of the FCC phase is higher than that of the BCC phase, indicating that the volume fraction of the FCC phase is higher than that of the BCC phase. A further observation is that the peak width of the deformed specimen is slightly larger than the peak width of the as-cast specimen. The cold-rolled specimen exhibits peaks similar to those of the as-cast specimen, though the intensity of the peaks differs significantly. Despite this, it is difficult to determine why this phenomenon occurs, as several factors, including instrumental effects, crystal sizes, lattice strain, and microstructural defects, may play a role. The breaks in dendrites and the dislocation density caused by severe plastic deformation are two possible factors that may contribute to peak widening. Moreover, there was no peak indicating the presence of an intermetallic compound.

3.2 Microstructural Evolutions

Figure 3(a) and (b) illustrates the specimen's microstructure in an as-cast state, demonstrating a typical dendritic structure. The microstructure comprises interdendritic (ID) and cellular-like dendrite regions (DR). Similar to the eutectic lamellar microstructure of $\text{AlCoCrFeNi}_{2.4}$ EHEA alloy, the microstructure of the ID regions of the $\text{AlCoCrFeNi}_{2.1}$ alloy is predominantly composed of typical hyper-eutectic structures (primary Laves phase and FCC + Laves phase eutectic) consisting of dark and light phases (Ref 32). There are two distinct phases in the as-cast structure. Dendritic regions include a $L1_2$ (FCC) phase and a B_2 (BCC) phase formed within the interdendritic structure. According to Fig. 2(c), when cold-rolled along the

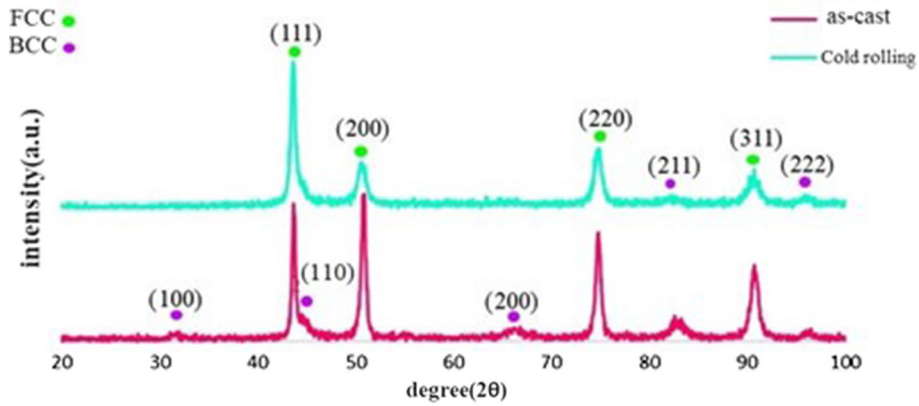


Fig. 2 XRD pattern of the $AlCoCrFeNi_{2.4}$ HEA in two different states

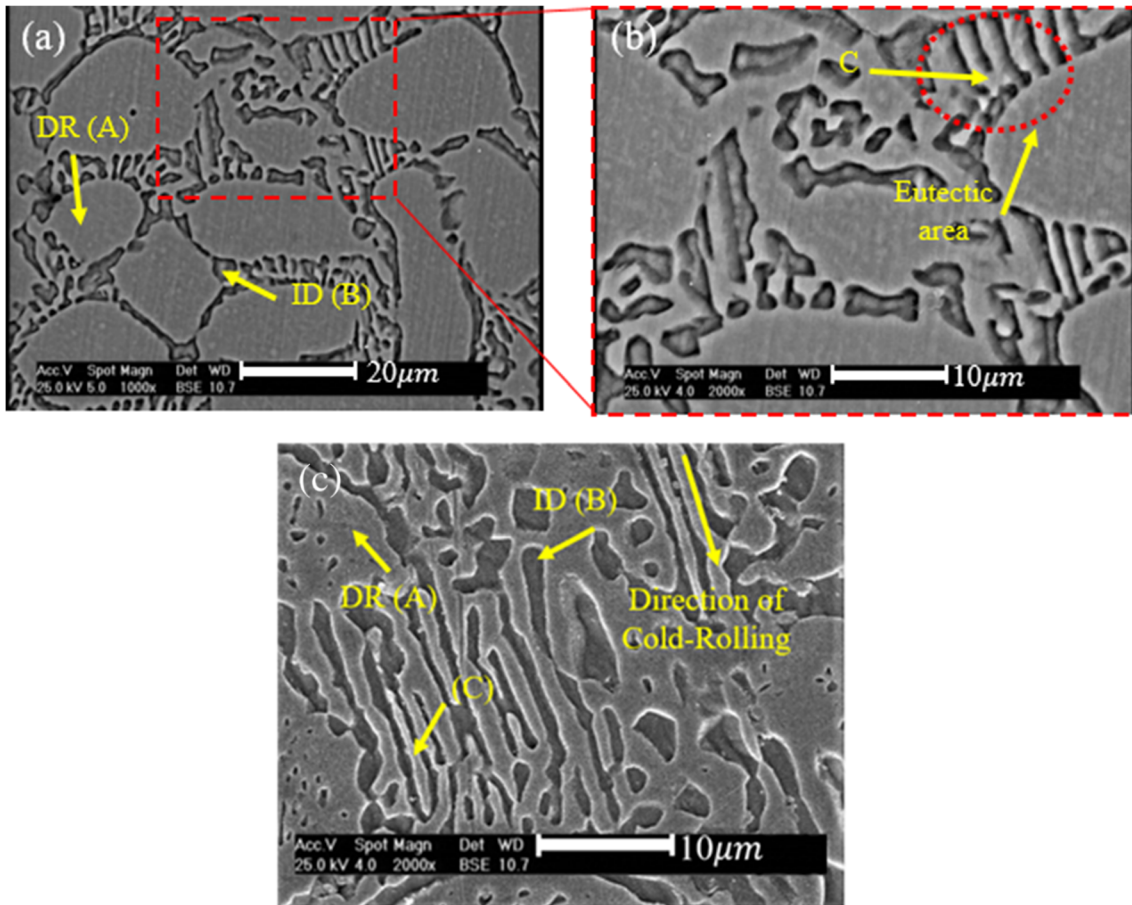


Fig. 3 SEM images with regard to the microstructure of the $AlCoCrFeNi_{2.4}$ alloy: (a) as-cast, (b) magnified across the interdendritic region in the as-cast state demonstrating eutectic structure, (c) cold-rolled by 90%

direction of the roll, the dendritic grains are elongated due to 90% deformation.

SEM micrographs show that coarse dendrites' microstructure improves when subjected to high levels of plastic deformation. As predicted, SEM analyses of the alloy revealed no secondary phases; the absence of secondary phases is likely due to a lack of long-range diffusion at room temperature. The EDS analysis (Table 2) and EDS maps (Fig. 4) of the $AlCoCrFeNi_{2.4}$ alloy reveals that the matrix phases in DR regions are deficient in Al, while the dark phase in ID regions is

rich in Ni and Al. Furthermore, Co, Cr, and Fe are uniformly distributed throughout the DR and ID regions of the $AlCoCrFeNi_{2.4}$ alloy. It is more likely that the fraction of the eutectic region is considerably lower than that of the primary solidified FCC phase.

3.3 Mechanical Behavior

Figure 5 illustrates the stress–strain curves for the $AlCoCrFeNi_{2.4}$ alloy in an as-cast and cold-rolled state. The details of yield strength (YS), ultimate tensile strength (UTS),

Table 2 EDS results of phases in two different states

Specimen	Phase, Point	Elements, at. %				
		Al	Cr	Co	Fe	Ni
As-cast	DR(A)	7.62	18.95	19.03	19.55	34.84
	ID(B)	15.00	12.98	15.25	10.77	45.31
	C	10.85	16.03	15.25	14.67	42.09
Cold-rolled	DR(A)	6.77	19.29	18.69	19.48	35.76
	ID(B)	18.12	8.70	12.88	9.72	39.79
	C	11.33	17.24	17.23	17.36	36.83

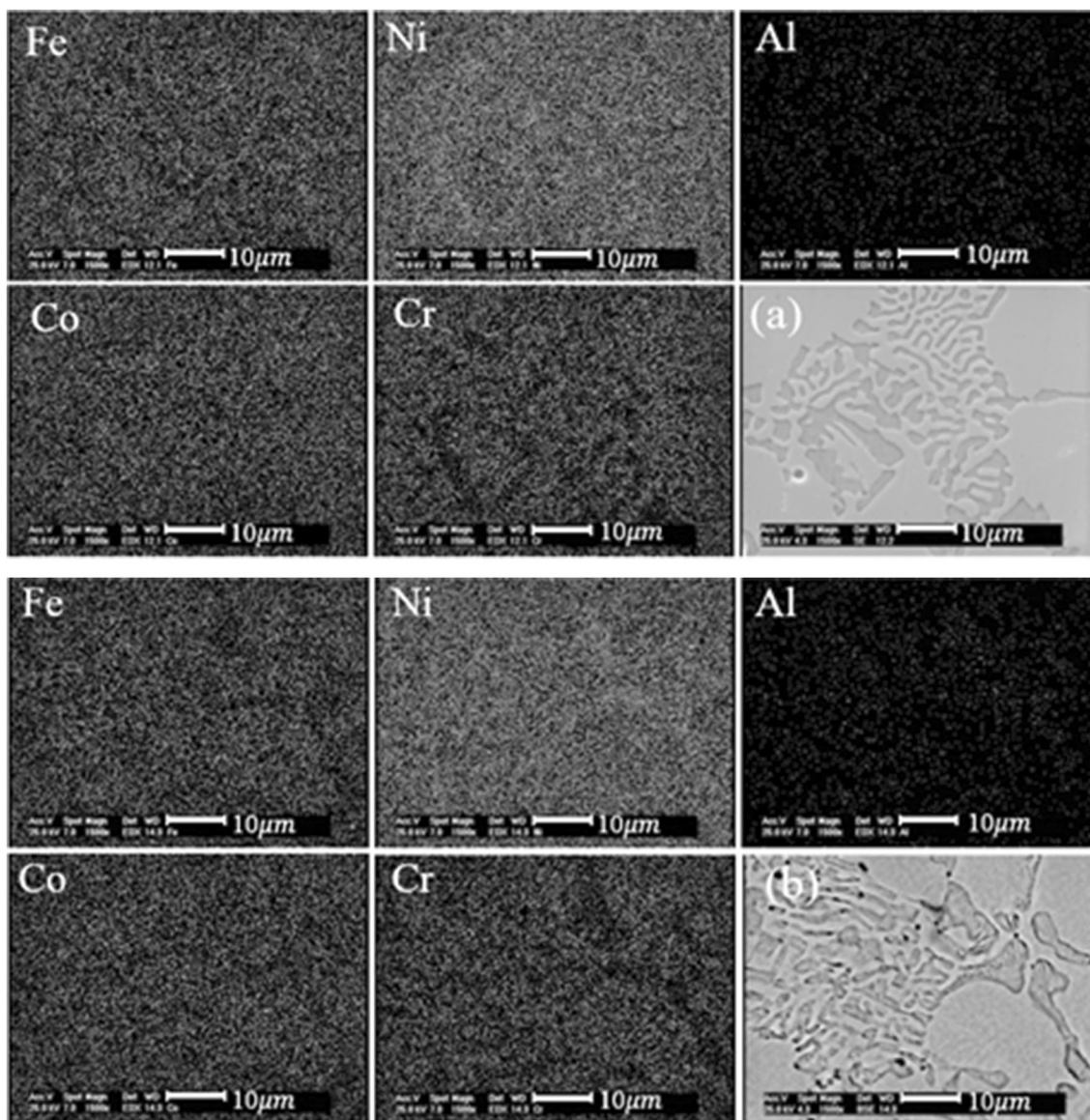


Fig. 4 BSE images and EDS maps of AlCoCrFeNi_{2.4} alloy: (a) as-cast, (b) cold-rolled by 90%

and fracture strain are summarized in Table 3. The studied alloy possesses desirable plasticity and elongation for the as-cast alloy, in addition to a notable yield strength of approximately 619 MPa. These properties for as-cast structures are intriguing, given that as-cast structures do not typically exhibit good mechanical properties. In the cold rolling condition, the alloy's

yield and ultimate strengths increased significantly compared to the as-cast state. Nonetheless, this was accomplished at the expense of ductility. Following a 90% reduction by cold rolling, the alloy's yield and tensile strengths increased significantly, reaching 1791 and 1956 MPa, respectively. The present study indicates that cold rolling is an effective

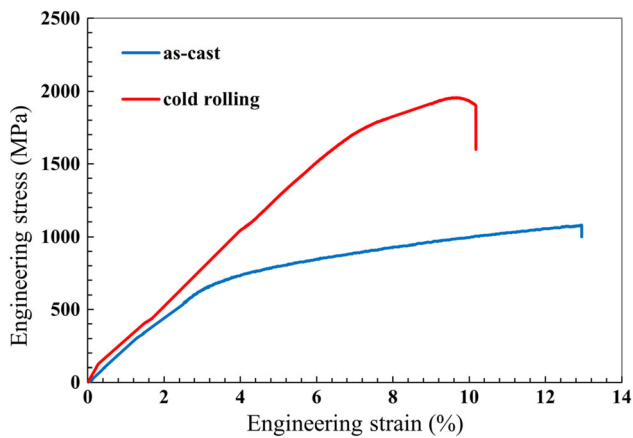


Fig. 5 Engineering tensile curves of AlCoCrFeNi_{2.4} HEA in the two states

Table 3 Mechanical characteristics of AlCoCrFeNi_{2.4} HEA in the two states

Specimen	σ_{YS} , MPa	σ_{UTS} , MPa	ϵ_f , %	Hardness, HV
As-cast	619	1078	13.07	288 ± 11
Cold-rolled	1791	1956	10.17	460 ± 13

technique for optimizing the mechanical properties of HEAs. In addition, it is noteworthy that the current HEA's high strength and good ductility make them an excellent candidate for structural applications.

As a result of the microstructural modification, decreasing grain size, and work hardening, the cold rolling process generally results in a significant increase in strength. This study determined that mechanically treating this alloy can be an effective method for improving its mechanical properties. According to Table 3, the cold-rolled specimen has a hardness of approximately 460 HV, which is approximately 1.6 times that of the as-cast condition (288 HV). The increase in hardness following cold rolling can be attributable to two primary causes. The compression stress refines the microstructure (by breaking down coarse dendrites and reducing grain size) and eliminates casting defects such as pores. The second reason relates to the severe network distortion caused by cold rolling, which can lead to solid solution strengthening and work hardening.

By cold rolling up to 90% of the thickness, the hardness can be increased by almost 60%. This behavior occurs as a result of dislocation density variations due to strain hardening during cold rolling. It is possible to measure the dislocation density of the samples using Eq 2 (Ref 33-36):

$$\rho = \frac{2\sqrt{3}\cdot\epsilon}{Db} \quad (\text{Eq 2})$$

where ϵ is the micro-strain, D is the crystallite size, and b is the Burgers vector. Crystallite size (D) and micro-strain (ϵ) of the alloy at different thickness reduction are calculated using MAUD software and XRD patterns.

Figure 6 and Table 4 display the results of shear punch tests conducted at room temperature on as-cast and cold-rolled AlCoCrFeNi_{2.4} alloy samples. According to these findings, the changes in shear yield stress between the as-cast and cold-

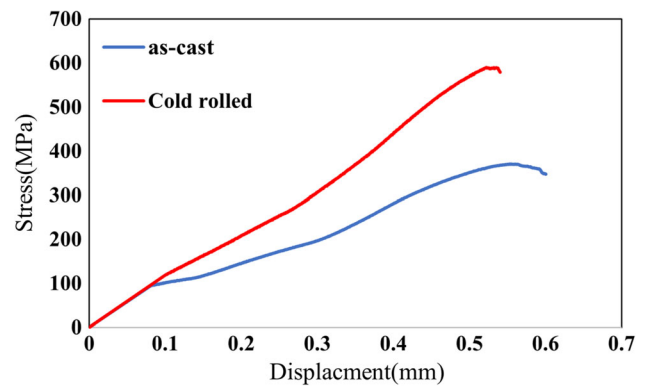


Fig. 6 Shear punch testing curves of AlCoCrFeNi_{2.4} HEA in as-cast and cold-rolled states under

Table 4 Shear property of AlCoCrFeNi_{2.4} HEA in the two states under room temperature

State	Shear yield stress, MPa	Ultimate shear stress, MPa
As-cast	223 ± 11	276 ± 12
Cold-rolled	331 ± 15	390 ± 13

Table 5 Dynamic parameters calculated by fitting liner curves to potentiodynamic polarization curves

Specimen	R_p , k. Cm ²	I_{corr} , $\mu\text{A}/\text{Cm}^2$	E_{corr} , mV
Cold-rolled	16.5	67	- 425
As-cast	56.3	36	- 294

rolled specimens are very similar to the changes in hardness (Table 3). In addition, the non-uniform deformation after the ultimate shear stress was greater in the as-cast state than in the cold-rolled state (Fig. 6). This indicates that the cold-rolled sample has a lower ductility.

3.4 Corrosion Behavior

Figure 7 depicts the potentiodynamic polarization curves for the studied alloy when scanned at a rate of 10 mV/s. The results in Table 5 indicate that the corrosion kinetic parameters can linearly describe the corrosion process. Consequently, it can be concluded that the higher the free corrosion potential, the lower the free corrosion current density, and the higher the linear polarization resistance of the surface, the greater the corrosion resistance (Ref 37-40).

The polarization curve in Fig. 7 clearly demonstrates a passivation zone with a larger area of active dissolution. Initially, the polarization curves in the activation region are relatively flat. As the corrosion potential rises, the curves become more pronounced. The steady-state passivation area appears related to the polarization current rise area. In this instance, there is only a slight change in the polarization current, which results in forming a passive film on the alloy's surface and increasing its corrosion resistance. As shown in Fig. 7, as-cast specimens have a higher corrosion potential (-294 mV) and a lower corrosion current density (36 $\mu\text{A}/\text{Cm}^2$) than cold-rolled specimens, which have a corrosion

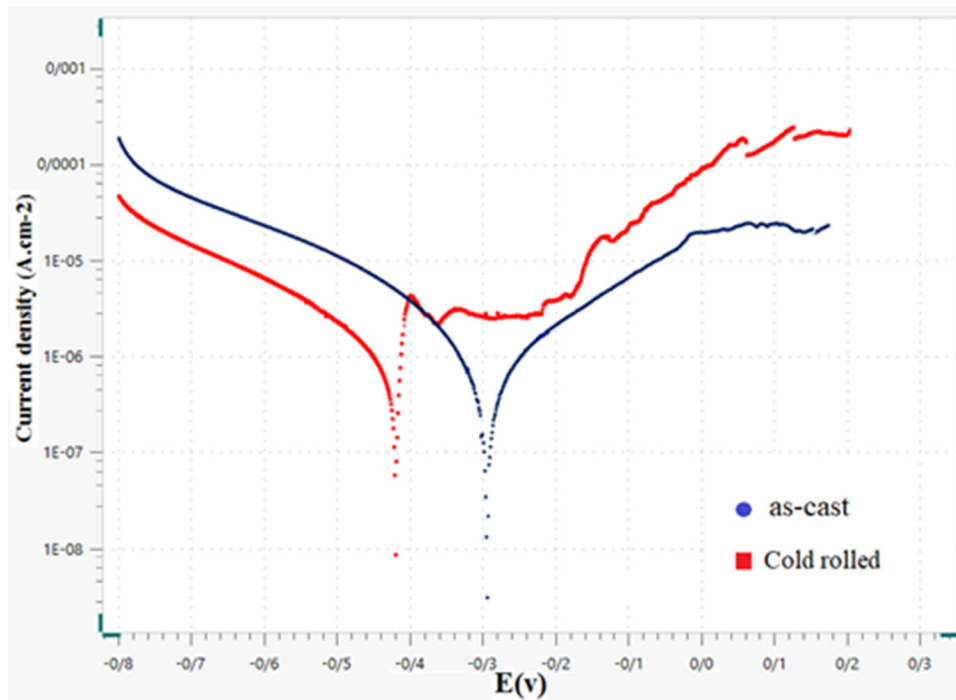


Fig. 7 Potentiodynamic polarization curves for AlCoCrFeNi_{2.4} high-entropy alloys in 3.5 Wt.% NaCl solution

potential of (−425 mV) and a corrosion current density of (67 $\mu\text{A}/\text{Cm}^2$). Therefore, when exposed to a NaCl corrosive environment, the as-cast specimen exhibited greater corrosion resistance than the cold-rolled specimen.

3.5 Fractography of Fractured Samples

Figure 8 depicts the fracture appearance of the samples following tensile testing at room temperature in both states. A characteristic dimple is visible on the as-cast specimen, indicating that it has undergone significant plastic deformation. In other words, the material broke in a ductile manner. Clearly, the as-cast sample has numerous dimples, although they are shallow, resulting in moderate elongation. There is no indication of brittle fracture on the surface of the as-cast specimen. In contrast, the cold-rolled sample exhibits dense small cleavage faces, indicating a semi-cleavage failure. This implies that the failure occurred without significant plastic deformation.

4. Conclusions

The cold rolling process was performed on AlCoCrFeNi_{2.4} HEA with a thickness reduction of up to 90% at room temperature. XRD and SEM techniques were used to characterize the microstructural evolutions. The hardness, shear, and tension properties were then assessed. In addition, the corrosion behavior of AlCoCrFeNi_{2.4} HEA was investigated. Based on the findings, the following conclusions were reached:

- The microstructure of as-cast alloy, including the oriented cellular structures, consists of NiAl-rich (B_2) and CoCrFe-Ni-rich ($L1_2$) phases.
- The tensile yield strength in the as-cast and cold-rolled states was approximately 831 and 1791 MPa, respectively. The shear yield strength increased from 223 MPa for the as-cast state to 331 MPa for the cold-rolled state. The alloy's hardness increases from 288 HV when as-cast to 460 HV after cold rolling.

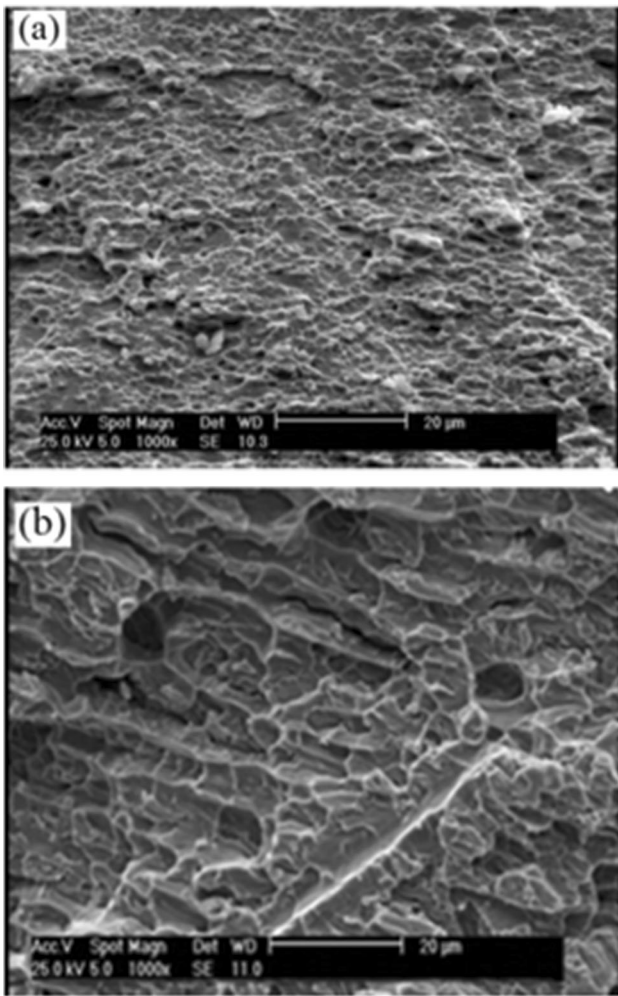


Fig. 8 SEM fractography of AlCoCrFeNi_{2.4} alloy in two states: (a) as-cast, (b) cold-rolled by 90%

- Both samples exhibit good corrosion resistance in a 3.5 wt.% NaCl solution; however, cold-rolled samples demonstrate superior corrosion performance.

References

- J.-W. Yeh, S.K. Chen, S.J. Lin, J.Y. Gan, T.S. Chin, T.T. Shun, C.H. Tsau, and S.Y. Chang, Nanostructured High-Entropy Alloys with Multiple Principal Elements: Novel Alloy Design Concepts and Outcomes, *Adv. Eng. Mater.*, 2004, **6**, p 299–303
- B. Cantor, I.T.H. Chang, P. Knight, and A.J.B. Vincent, Microstructural Development Inequiatomic Multicomponent Alloys, *Mater. Sci. Eng. A.*, 2004, **375–377**, p 213–218
- Z. Li, K.G. Pradeep, Y. Deng, D. Raabe, and C.C. Tasan, Metastable High-Entropy Dual-Phase Alloys Overcome the Strength-Ductility Trade-Off, *Nature*, 2016, **534**, p 227–230
- A. Ghaderi, H. Moghanni, and K. Dehghani, Microstructural Evolution and Mechanical Properties of Al_{0.5}CoCrFeNi High-entropy Alloy After Cold Rolling and Annealing Treatments, *J. Mater. Eng. Perform.*, 2021, **30**, p 1–9
- M.C. Gao, J.-W. Yeh, P.K. Liaw, and Y. Zhang Eds., *High-entropy alloys*. Springer International Publishing, Cham, 2016
- H. Fu, H. Zhao, S. Song, Z. Zhang, and J. Xie, Evolution of the Cold-Rolling and Recrystallization Textures in FeNiCoAlNbB Shape Memory Alloy, *J. Alloys Compd.*, 2016, **686**, p 1008–1016
- Z. Fu, L. Jiang, J.L. Wardini, B.E. MacDonald, H. Wen, W. Xiong, D. Zhang, Y. Zhou, T.J. Rupert, W. Chen, and E.J. Lavermia, A High-Entropy Alloy with Hierarchical Nanoprecipitates and Ultrahigh Strength, *Sci. Adv.*, 2018, **4**, p e8712
- Y. Zou, S. Maiti, W. Steurer, and R. Spolenak, Size-Dependent Plasticity in an Nb₂₅Mo₂₅Ta₂₅W₂₅ Refractory High-Entropy Alloy, *Acta Mater.*, 2014, **65**, p 85–97
- C.W. Tsai, M.H. Tsai, J.W. Yeh, and C.C. Yang, Effect of Temperature on Mechanical Properties of Al_{0.5}CoCrCuFeNi Wrought Alloy, *J. Alloys Compd.*, 2010, **490**, p 160–165
- O.N. Senkov, J.M. Scott, S.V. Senkova, D.B. Miracle, and C.F. Woodward, Microstructure and Room Temperature Properties of a High-Entropy TaNbHfZrTi Alloy, *J. Alloys Compd.*, 2011, **509**, p 6043–6048
- A. Gali and E.P.P. George, Tensile Properties of High- and Medium-Entropy Alloys, *Intermetallics*, 2013, **39**, p 74–78
- F. Otto, A. Dlouhý, C. Somsen, H. Bei, G. Eggeler, and E.P.P. George, The Influences of Temperature and Microstructure on the Tensile Properties of a CoCrFeMnNi High-Entropy Alloy, *Acta Mater.*, 2013, **61**(5743), p 5755
- J.Y. He, W.H. Liu, H. Wang, Y. Wu, X.J. Liu, T.G. Nieh, and Z.P. Lu, Effects of Al Addition on Structural Evolution and Tensile Properties of the FeCoNiCrMn High-Entropy Alloy System, *Acta Mater.*, 2014, **62**, p 105–113
- Y. Zou, S. Maiti, W. Steurer, and R. Spolenak, Size-Dependent Plasticity in an Nb₂₅Mo₂₅Ta₂₅W₂₅ Refractory High-Entropy Alloy, *Acta Mater.*, 2014, **65**, p 85–97
- M. Wang, L. Yiping, T. Wang, C. Zhang, Z. Cao, T. Li, and P.K. Liaw, A Novel Bulk Eutectic High-Entropy Alloy with Outstanding as-cast Specific Yield Strengths at Elevated Temperatures, *Scr. Mater.*, 2021, **204**, p 114132
- M.J. Yao, K.G. Pradeep, C.C. Tasan, and D. Raabe, A Novel Single Phase Non-Equiatomic FeMnNiCoCr High-Entropy Alloy with Exceptional Phase Stability and Tensile Ductility, *Scr. Mater.*, 2014, **72–73**, p 5–8
- Y.Y. Chen, U.T. Hong, J.W. Yeh, and H.C. Shih, Selected Corrosion Behaviors of a Cu_{0.5}NiAlCoCrFeSi Bulk Glassy Alloy in 288 °C High-Purity Water, *Scr. Mater.*, 2006, **54**, p 1997–2001
- Y.X. Wang, Y.J. Yang, H.J. Yang, M. Zhang, S.G. Ma, and J.W. Qiao, Microstructure and Wear Properties of Nitrided AlCoCrFeNi High-Entropy Alloy, *Mater. Chem. Phys.*, 2017, **210**, p 233
- Mingliang Wang, Lu. Yiping, Guojia Zhang, Hongzhi Cui, Xu. Dingfeng, Na. Wei, and Tingju Li, A Novel High-Entropy Alloy Composite Coating with Core-Shell Structures Prepared by Plasma Cladding, *Vacuum*, 2021, **184**, p 109905
- B. Gludovatz, A. Hohenwarter, D. Catoor, E.H. Chang, E.P. George, and R.O. Ritchie, A Fracture-Resistant High-Entropy Alloy for Cryogenic Applications, *Science*, 2014, **345**, p 1153–1158
- L. Zhang, Y. Zhou, X. Jin, X.Y. Dua, and B.S. Li, The Microstructure and High-Temperature Properties of Novel Nano Precipitation-Hardened Face Centered Cubic High-Entropy Superalloys, *Scr. Mater.*, 2018, **146**, p 226–230
- X.Z. Gao, Y.P. Lu, B. Zhang, N.N. Liang, G.Z. Wu, G. Sha, J.Z. Liu, and Y.H. Zhao, Microstructural Origins of High Strength and High Ductility in an AlCoCrFeNi₂₁ Eutectic High-Entropy Alloy, *Acta Mater.*, 2017, **141**, p 59–66
- Z.M. Li, K.G. Pradeep, Y. Deng, D. Raabe, and C.C. Tasan, Metastable High-Entropy Dual-Phase Alloys Overcome the Strength-Ductility Trade-off, *Nature*, 2016, **534**, p 227–234
- Y. Lu, Y. Dong, S. Guo, L. Jiang, H. Kang, T. Wang, B. Wen, Z. Wang, J. Jie, and Z. Cao, A Promising New Class of High-Temperature Alloys: Eutectic High-Entropy Alloys, *Sci. Rep.*, 2014, **4**, p 6200
- I.S. Wani, T. Bhattacharjee, S. Sheikh, Y.P. Lu, S. Chatterjee, P. Bhattacharjee, S. Guo, and N. Tsuji, Ultrafine-Grained AlCoCrFeNi_{2.1} Eutectic High-Entropy Alloy, *Mater. Res. Lett.*, 2016, **4**(3), p 174–179
- I.S. Wani, T. Bhattacharjee, S. Sheikh, Y.P. Lu, S. Chatterjee, P.P. Bhattacharjee, S. Guo, and N. Tsuji, Ultrafine-Grained AlCoCrFeNi_{2.1} Eutectic High-Entropy Alloy, *Mater. Res. Lett.*, 2016, **4**, p 174–179
- S. Guo, C. Ng, J. Lu, and C.T. Liu, Effect of Valence Electron Concentration on Stability of FCC or BCC Phase in High Entropy Alloys, *J. Appl. Phys.*, 2011, **109**, p 103505

28. S.G. Ma, Z.D. Chen, and Y. Zhang, Evolution of Microstructures and Properties of the Al_xCrCuFeNi₂ High-Entropy Alloys, *Mater. Sci. Forum*, 2013, **745–746**, p 706–714
29. Y. Lu, X. Gao, L. Jiang, Z. Chen, T. Wang, J. Jie, H. Kang, Y. Zhang, S. Guo, H. Ruan, Y. Zhao, Z. Cao, and T. Li, Directly Cast Bulk Eutectic and Near-Eutectic High Entropy Alloys with Balanced Strength and Ductility in a Wide Temperature Range, *Acta Mater.*, 2017, **124**, p 143–150
30. Y. Zhang, X. Wang, J. Li, Y. Huang, Y. Lu, and X. Sun, Deformation Mechanism During High-Temperature Tensile Test in an Eutectic High-Entropy Alloy AlCoCrFeNi_{2.1}, *Mater. Sci. Eng. A*, 2018, **724**, p 148–155
31. Y.F. Wang, S.G. Ma, X.H. Chen, J.Y. Shi, Y. Zhang, and J.W. Qiao, Optimizing Mechanical Properties of AlCoCrFeNiTi_x High-Entropy Alloys by Tailoring Microstructures, *Acta Metall Sin*, 2013, **26**, p 277–284
32. L. Cao, X. Wang, Y. Wang, L. Zhang, Y. Yang, F. Liu, and Y. Cui, Microstructural Evolution, Phase Formation and Mechanical Properties of Multi-component AlCoCrFeNi_x Alloys Microstructural Evolution, Phase Formation and Mechanical Properties of Multi-component AlCoCrFeNi_x Alloys, *Appl. Phys. A*, 2019, **125**, p 699–704
33. J. Hou, M. Zhang, S. Ma, P.K. Liaw, Y. Zhang, and J. Qiao, Strengthening in Al_{0.25}CoCrFeNi High-Entropy Alloys by Cold Rolling, *Mater. Sci. Eng. A*, 2017, **707**, p 593–601
34. H. Pal, A. Chanda, and M. De, Characterisation of microstructure of isothermal martensite in Fe–23Ni–3.8Mn by Rietveld method, *J. Alloys Compd.*, 1998, **278**, p 209–215
35. A. Chanda and M. De, X-ray Characterization of the Microstructure of α -CuTi Alloys by Rietveld's method, *J. Alloys Compd.*, 2000, **313**, p 104–114
36. G. Dini, R. Ueji, A. Najafizadeh, and S.M. Monir-Vaghefi, Flow Stress Analysis of TWIP Steel via the XRD Measurement of Dislocation Density, *Mater. Sci. Eng. A*, 2010, **527**, p 2759–2763
37. T.T. Shun, C.H. Hung, and C.F. Lee, The Effects of Secondary Elemental Mo or Ti addition in Al_{0.3}CoCrFeNi High-Entropy Alloy on Age Hardening at 700 °C, *J. Alloys Compd.*, 2010, **495**, p 55–58
38. X.F. Wang, Y. Zhang, Y. Qiao, and G.L. Chen, Novel Microstructure and Properties of Multicomponent CoCrCuFeNiTi_x Alloys, *Intermetallics*, 2007, **15**, p 357–362
39. J. Dutkiewicz, L. Jaworska, W. Maziarz, T. Czeppe, M. Lejkowska, A. Kubicek, and M. Pasternak, Consolidation of Amorphous Ball-Milled Zr–Cu–Al and Zr–Ni–Ti–Cu Powders, *J. Alloys Compd.*, 2007, **434**, p 333–335
40. Y.F. Kao, T.D. Lee, S.K. Chen, and Y.S. Chang, Electrochemical Passive Properties of Al_xCoCrFeNi (x = 0, 0.25, 0.50, 1.00) Alloys in Sulfuric Acids, *Corros. Sci.*, 2010, **52**, p 1026–1034

Publisher's Note Springer Nature remains neutral with regard to jurisdictional claims in published maps and institutional affiliations.

Springer Nature or its licensor (e.g. a society or other partner) holds exclusive rights to this article under a publishing agreement with the author(s) or other rightsholder(s); author self-archiving of the accepted manuscript version of this article is solely governed by the terms of such publishing agreement and applicable law.